Magnitude- and Shape-Related Feature Integration in Hyperspectral Mixture Analysis to Monitor Weeds in Citrus Orchards

Ben Somers, *Student Member, IEEE*, Stephanie Delalieux, Willem W. Verstraeten, Jan Verbesselt, Stefaan Lhermitte, and Pol Coppin

***Abstract*—Traditionally, spectral mixture analysis (SMA) fails to fully account for highly similar ground components or endmembers. The high similarity between weed and crop spectra hampers the implementation of SMA for steering weed control management practices. To address this problem, this paper presents an alternative SMA technique, referred to as Integrated Spectral Unmixing (InSU). InSU combines both magnitude (i.e., reflectance) and shape (i.e., derivative reflectance) related features in an automated waveband selection protocol. Analysis was performed on different simulated mixed pixel spectra sets compiled from *in situ*-measured weed canopy, *Citrus* canopy, and soil spectra. Compared to traditional linear SMA, InSU significantly improved weed cover fraction estimations. An average decrease in fraction abundance error (Δf) of 0.09 was demonstrated for a signal-to-noise ratio (SNR) of 500 : 1, while for a SNR of 50 : 1, the decrease was 0.06.**

***Index Terms*—Derivatives, endmember similarity, hyperspectral, spectral mixture analysis (SMA), stable feature selection, weighted least squares (LS).**

I. Introduction

THE SUCCESSFUL delineation of weed patches in agricultural fields creates a potential for the site-specific application of herbicides, resulting in subsequent ecological and economic benefits [1]. In this light, hyperspectral remote sensing has commonly been considered as an effective technique as variations in plant canopy spectral responses are indicative to changes in weed growth patterns [2], [3]. Remotely sensed images allow for a systematic and global coverage of the targeted area, which is a crucial benefit over labor-intensive and generally sample-based *in situ* monitoring systems [2], [4].

However, the success of remote-sensing-based agricultural weed detection is limited [3]. Most of the applied classification algorithms and vegetation indices suffer from the spectral admixture of ground components (e.g., crop and soil) other than the object of interest, in this case, weeds [2], [3]. To address this problem, some authors proposed the use of linear spectral mixture analysis (LSMA) [3], [5]. LSMA is a comprehensive image analysis technique that allows for subpixel classification [6]. Its potential is huge as the approach was shown effective in removing soil background effects from images containing mixed reflectance spectra (e.g., [7]–[11]). However, in a post emergence crop setting, conventional LSMA techniques still fail to fully differentiate among the highly similar spectral characteristics of weeds and crops (e.g., [2], [3], and [12]–[14]). Only a limited number of reports on the application of LSMA in agricultural remote sensing are available, and they only report suboptimal classification results [3], [5], [9], [15]. The residual errors in fraction estimates are generally attributed to the high spectral similarity between weeds and crops, and the spatial and temporal changes in (bio)physical and (bio)chemical conditions of the different land cover types [5], [9]. Additionally, the multiple scattering of photons between different surface components violates the linearity assumption of mixture models and, as such, induce residual errors in LSMA [9], [16], [17]. Nevertheless, the majority of vegetation monitoring studies neglects the effect of multiple scattering. LSMA is still applied given the simplicity and the relative accuracy of the linear models [9], [15].

The main objective of this paper is to present an alternative LSMA technique to address the ground component or endmember similarity problem. In our modified approach, original and derivative reflectance data are considered simultaneously in one single analysis. As such, an improved description of both the magnitude and shape of ground component spectra becomes feasible. An automated waveband selection protocol tracks the spectral features with the lowest similarity. The selected subset is incorporated in the analysis to improve subpixel fraction estimates. The algorithm was used to estimate weed cover fractions from a set of simulated data sets compiled from various mixtures of *in situ*-measured weed canopy, *Citrus* tree canopy, and bare soil spectra.

Manuscript received September 29, 2008; revised February 17, 2009 and April 8, 2009. First published August 18, 2009; current version published October 28, 2009. This work was supported by the Institute for the Promotion of Innovation through Science and Technology in Flanders (IWT-Vlaanderen).

B. Somers, W. W. Verstraeten, and P. Coppin are with the Department of Biosystems, M3-BIORES, Katholieke Universiteit Leuven, 3001 Leuven, Belgium (e-mail: ben.somers@biw.kuleuven.be; willem.verstraeten@biw.kuleuven.be; pol.coppin@biw.kuleuven.be).

S. Delalieux is with the Centre for Remote Sensing and Earth Observation processes (TAP), Flemish Institute for Technological Research (VITO), 2400 Mol, Belgium (e-mail: stephanie.delalieux@biw.kuleuven.be).

J. Verbesselt is with the Commonwealth Scientific and Industrial Research Organisation Sustainable Ecosystems, Clayton South, Vic. 3169, Australia (e-mail: Jan.VerBesselt@csiro.au).

S. Lhermitte is with the Centro de Estudios Avanzados en Zonas Aridas (CEAZA), Universidad de la Serena, 172-0170 La Serena, Chile (e-mail: stef.lhermitte@gmail.com).

Color versions of one or more of the figures in this paper are available online at http://ieeexplore.ieee.org.

Digital Object Identifier 10.1109/TGRS.2009.2024207

0196-2892/$26.00 © 2009 IEEE

Authorized licensed use limited to: UNIVERSIDAD DE LA SERENA. Downloaded on October 26, 2009 at 07:46 from IEEE Xplore. Restrictions apply.

II. Theoretical Background

A. LSMA

In LSMA, the observed spectrum r for any given pixel in the scene is expressed as

$$r = Mf + \varepsilon \quad \text{with} \sum_{j=1}^{m} f_j = 1 \text{ and } 0 \leq f_j \leq 1 \qquad (1)$$

where M is a matrix in which each column corresponds to the spectral signal of a specific ground cover class or endmember, and f is a column vector $[f_1, \ldots, f_m]^T$ that denotes the subpixel cover fractions occupied by each of the m endmembers [6]. The part of the spectrum that cannot be modeled is expressed as a residual term ε. The coefficients in (1) are constrained to 1) sum to one and 2) be nonnegative in order to obtain physically interpretable cover fraction estimates [18], [19].

The success of LSMA depends on the accuracy of the selection of the endmember spectral signatures [20]. Endmember spectra can either be extracted from the imagery itself (e.g., [21]–[26]) or derived from spectral libraries built from field or laboratory measurements [7]–[9]. Endmember spectra from field or laboratory measurements can be controlled well and measured accurately, yet, they may not match those in the image due to differences in sensors, atmospheric effects, and illumination conditions [20], [27]. The image endmember approach has its advantages and problems as well. Image endmembers are often obtained from the pure endmember pixels in the image to be unmixed. This is ideal since endmembers, as such, are selected as they are actually presented in the area. However, obtaining image endmembers' signatures can sometimes be difficult as the selection of image endmembers requires the availability of pixels comprised purely of each dominant cover type [20]. Image endmember extraction techniques therefore often fail to account for the spectral variability present within the different ground cover or endmember classes. This problem is less pronounced by using spectral libraries built from field measurements [7]–[9]. It is acknowledged that in remote locations, the collection of field spectra is sometimes not feasible. However, in an agricultural setting, it is likely feasible. In [26], an interesting technique is presented to construct endmember bundles from image data expressing as such the spectral variability within the different endmember classes.

Once the endmembers and their spectral signatures have been determined, subpixel cover distribution maps can be generated using approaches such as Gramm–Schmidt orthogonalization [28], maximum-likelihood [13], or least squares (LS) regression analysis [19]. This latter approach is used in this paper. Subpixel endmember fractions for the corresponding vector f are obtained by minimizing the following equation:

$$\sum_{i=1}^{n} \varepsilon_i = \sum_{i=1}^{n} \left(\sum_{j=1}^{m} (M_{i,j} \times f_j) - r_i \right)^2 \qquad (2)$$

where n is the number of available spectral bands [19].

B. Endmember Variability

The most profound source of error in LSMA lies in the lack of the ability to account for sufficient temporal and spatial spectral variability [7], [19], [26]. In a conventional LSMA approach, image-wide endmember spectra are defined. The natural variability within endmember classes is, as such, not accounted for, and this results in significant fraction estimate errors. Over the past decades, different approaches to negate the "fixed endmember" restriction have been presented and successfully tested in both natural and urban environments (e.g., [11], [14], [26], and [29]–[34]).

The following two types of variability are commonly distinguished: 1) the variability within an endmember class (intraclass variability) and 2) the similarity among endmember classes (interclass variability) [35]. The intraclass variability is linearly and negatively correlated with the accuracy of subpixel fraction estimates provided by LS spectral unmixing [13], [19]. In vegetation monitoring studies, the high similarity among reflectance spectra of different vegetation types [35], [36] provides an additional difficulty to obtain accurate classification results. Similarity between endmembers leads to a high correlation between the columns in the endmember matrix (M), which, in turn, leads to an unstable inverse matrix and a dramatic drop in estimate accuracy [13], [19], [37], [38]. The problem has been discussed by several authors [7], [8], [12], but only limited solutions have been proposed. Asner and Lobell [8] used a spectral tying transformation to emphasize endmember specific absorption features. Tying involves subtraction of reflectance at one waveband (the tie point) from all other wavebands. Although successful in semiarid regions [8], the approach failed to improve the decomposition of soil–vegetation mixtures under moist soil conditions [11]. In addition, no attempts were made to separate spectral mixtures composed of different vegetation types.

C. Derivative SMA

Derivative analysis has previously been revealed as an interesting approach to deal with spectral similarity. The derivatives of a spectrum highlight changes in the shape of the original spectrum and are not sensitive to the spectral magnitude [31], [37]. First-derivative spectra are informative on the slope of the original spectra while second derivatives allow identifying inflection points [39].

The integration of derivative analysis and LSMA was proposed by Zhang *et al.* [31], who presented derivative spectral unmixing (DSU), in which derivative endmember spectra were used to emphasize the interclass variability while reducing the intraclass variability. In DSU, the linear mixture model (1) is rewritten as

$$\frac{d^t r_i}{di^t} = f \times \frac{d^t M_i}{di^t} + \varepsilon \qquad (3)$$

where $(d^t r_i / di^t)$ and $(d^t M_i / di^t)$ are the tth derivative of the spectrum of the mixed pixel and the endmember matrix M at wavelength i, respectively. A DSU approach using second-derivative endmember spectra was successfully applied to map the distribution of rock-encrusting lichen communities in Jasper, Canada [31]. Recently, a similar approach using first derivatives was applied to estimate the partial abundance of

Authorized licensed use limited to: UNIVERSIDAD DE LA SERENA. Downloaded on October 26, 2009 at 07:46 from IEEE Xplore. Restrictions apply.

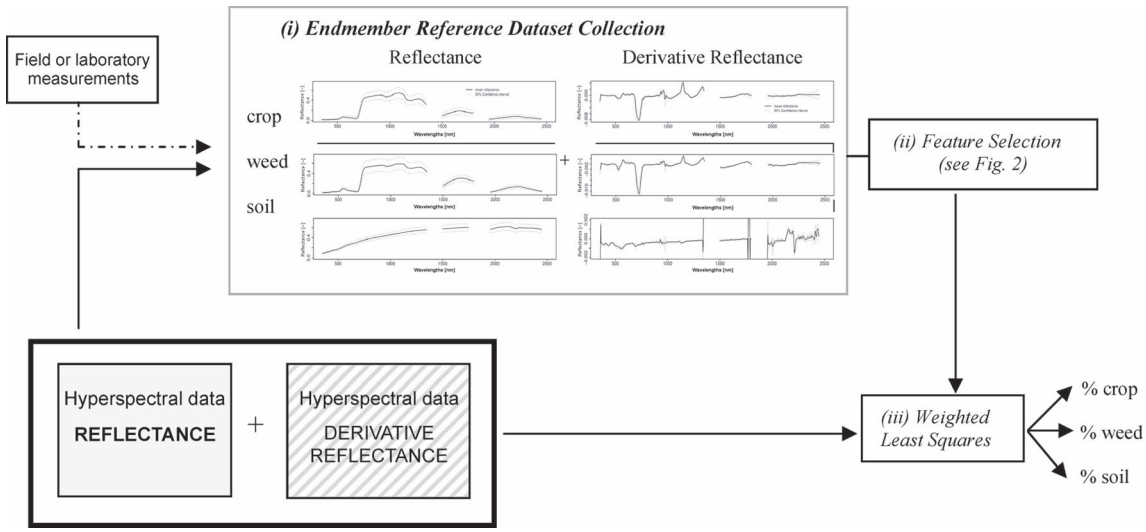

Fig. 1. Schematic overview of the InSU. First, an endmember spectral data set, either extracted directly from hyperspectral data itself or derived from field or laboratory measurements, is collected for each of the target endmembers. (i) Both original reflectance and derivative spectra are calculated. (ii) An automated protocol selects the most appropriate spectral features allowing for the best possible separation among the presented endmembers. (iii) The selected set of optimal spectral features is used in a weighted LS mixture analysis to generate from the hyperspectral data (mixed pixels, bold square) the corresponding subpixel spatial distribution maps.

spectrally similar iron-bearing oxide/hydroxide/sulfate minerals in complex (simulated) mixtures [37]. Despite its potential, no reports were found on the validation of DSU in other ecosystems.

D. Integrated Spectral Unmixing (InSU)

To optimize the discrimination between endmember spectra, we propose to integrate both original and derivative reflectance data in one SMA. This approach, referred to as InSU, is founded on the following three key elements: 1) an adapted mixture model; 2) a weighted LS inversion algorithm; and 3) an automated waveband selection protocol. A schematic overview of the proposed algorithm is shown in Fig. 1. The next paragraphs give a theoretical background on each of the elementary steps.

1) Mixture Model: The integrated mixing model is the same as reflectance/derivative mixing models described in (1) and (3) apart from the LS regression estimator that will rely on both (1) and (3) to estimate f. Consequently, the mixture model could be defined as

$$\begin{bmatrix} r_i \\ \frac{d^t r_i}{di^t} \end{bmatrix} = f \times \begin{bmatrix} M_i \\ \frac{d^t M_i}{di^t} \end{bmatrix} + \varepsilon_i. \tag{4}$$

Both first and second derivatives can be included in the model. First derivatives are calculated as $(d^t M_i/di^t) = r_i - r_{i+1}$ and second derivatives as $(d^2 M_i/di^2) = (dr_i/di) - (dr_{i+1}/di)$.

2) Weighted LS: Inversion of the mixture model implies the minimization of the LS error (LSE). Typically, the LSE is equally weighted for all wavebands or spectral features, assuming equal important contributions on LSE [19]. Although some authors question this approach even when only original reflectance features are used [14], the assumption certainly does not hold when reflectance and derivative spectra are included in one analysis. $\sum_{i=1}^{n} \varepsilon_{\text{derivative},i}$ compared to $\sum_{i=1}^{n} \varepsilon_{\text{reflectance},i}$ is relatively small (i.e., a factor 1000 and 1 000 000 for first and second derivatives, respectively). This implies that the LS estimator, which minimizes $(\sum_{i=1}^{n}(\varepsilon_{\text{reflectance},i} + \varepsilon_{\text{derivative},i}))$ [see (2)] within the constraints of (1), is mainly determined by the original reflectance features, while the contribution of the derivatives to the LS solution is negligible to nonexistent.

To circumvent this problem, model inversion was performed using a weighted LS regression approach, adapted from [14]. A weighing vector w is introduced into (4) and is used to equalize the contribution of the derivative and original reflectance features in the mixture analysis. w scales the reflected energy in feature $(d^t r_i/di^t)$ as follows:

$$w = \bar{r} \Big/ \frac{d^t \bar{r}}{di^t} \tag{5}$$

where $\bar{r}$ and $(d^t \bar{r}/di^t)$ are the spectrum-wide averages of the original and tth-derivative reflectance of the considered mixture, respectively. w preserves endmember variability among endmember classes but gives reflectance and derivatives an equal weight in LSE calculations.

3) Feature Selection: According to [8], [10], and [34], the variability within endmember classes can be significantly reduced if one focuses on a subset of wavelengths or spectral features. Based on this assumption, an automated feature selection algorithm [34] is used to select a spectral subset that provides optimal cover fraction estimations. The spectral features most sensitive to spectral endmember variability are removed from the analysis, and this tends to increase the overall accuracy. A detailed description of the algorithm can be found in [34], but the concept can be summarized in two steps.

First, the features' sensitivity toward spectral variability is assessed using the InStability Index (ISI) criterion [14], [34]. ISI is defined as the ratio of the intraclass (i.e., the sum of the endmember class standard deviations) to the interclass endmember variability (i.e., average Euclidean distance between the class means), i.e.,

$$\text{ISI}_i = \frac{2}{m \times (m-1)} \sum_{z=1}^{m-1} \sum_{j=z+1}^{m} \frac{\sigma_{i,z} + \sigma_{i,j}}{|x_{\text{mean},i,z} - x_{\text{mean},i,j}|} \tag{6}$$

Authorized licensed use limited to: UNIVERSIDAD DE LA SERENA. Downloaded on October 26, 2009 at 07:46 from IEEE Xplore. Restrictions apply.

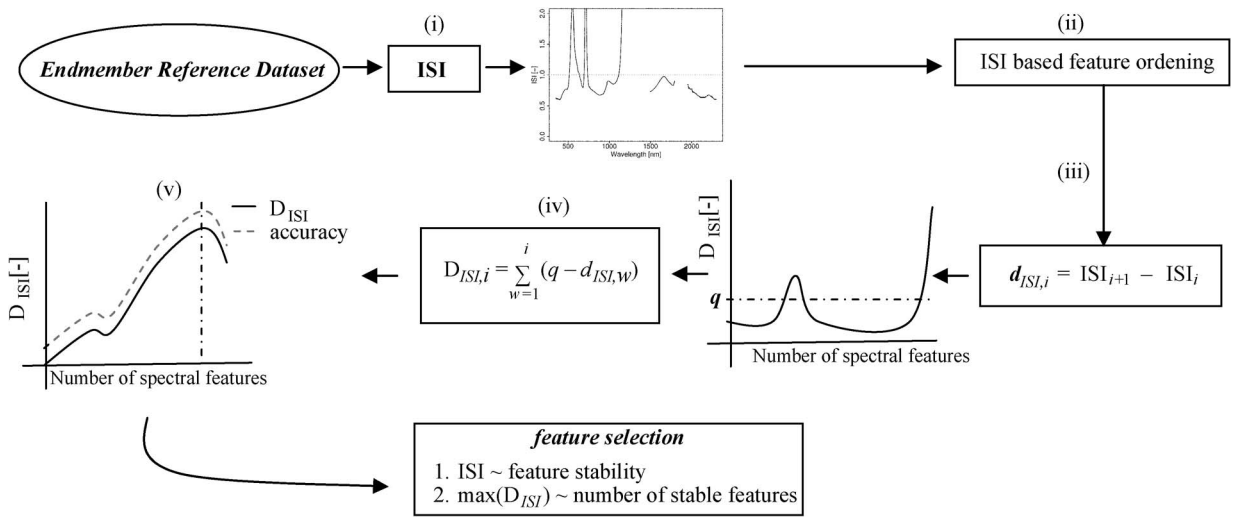

Fig. 2. Schematic overview of the automated feature selection algorithm. Based on the available spectral endmember data sets, the sensitivity of each spectral feature is determined by calculating the ISI. (i) ISI accounts for both the variability within and the similarity among endmember classes. (ii) All spectral features are ordered according to increasing ISI values. (iii) The difference in ISI among consecutive features $(d_{\mathrm{ISI},i})$ is calculated and then (iv) evaluated against the tradeoff point q (i.e., 0.015) $(D_{\mathrm{ISI},i})$. (v) $D_{\mathrm{ISI},i}$ models the trend in classification accuracy, and its maximum indicates the number of features needed for optimal cover fractions estimations.

where $x_{\mathrm{mean},i,z}$, $x_{\mathrm{mean},i,j}$, $\sigma_{i,z}$, and $\sigma_{i,j}$ are the mean reflectance or derivative spectra and standard deviations at wavelength i for endmember classes z and j, respectively, and m represents the number of endmembers in the scene. Note that ISI requires information on intraclass variability. The available endmember data set, as such, should be representative of the spectral variability present within the scene.

Second, spectral information is inevitably lost by removing features from the analysis. Therefore, if the aim is to obtain optimal cover fraction estimates, then a tradeoff is required between the number of spectral features included in the analysis (i.e., information) and the average ISI of the considered features (i.e., endmember variability, noise). The tradeoff protocol, illustrated in Fig. 2, is summarized as follows: 1) All available spectral features are ordered according to increasing ISI values. 2) The relative change in ISI between successive features $(d_{\mathrm{ISI},i})$ is calculated and evaluated against a tradeoff point. The tradeoff point is the value of $d_{\mathrm{ISI},i}$ at which fraction estimate accuracy does not change when additional spectral features are removed from the mixture analysis. For $d_{\mathrm{ISI},i} < q$, accuracy drops when additional features are removed, and the opposite is true for $d_{\mathrm{ISI},i} > q$. Previous research indicated 0.015 (i.e., q) to be a robust tradeoff point [34]. 3) The accumulated $d_{q,i}$ (i.e., difference between q and $d_{\mathrm{ISI},i}$) curve is calculated $(D_{\mathrm{ISI},i})$. $d_{q,i}$ quantifies the amplitude by which fraction estimate accuracy increases/decreases by removing additional spectral features from the mixture analysis. The actual SMA accuracy is not known in an operational application, although previous research [34] demonstrated a consistent resemblance between the trend in $D_{\mathrm{ISI},i}$ and the SMA accuracy for a set of urban and natural environments under differing conditions. Consequently, $D_{\mathrm{ISI},i}$ models the trend in SMA accuracy and its maximum indicates the number of features needed for optimal cover fraction estimations.

In InSU, the selected set of stable spectral features can be composed of both original and/or derivative (both first and second order) reflectance values.

III. Experimental Methodology and Simulated Data

A. Hyperspectral Data Sets

In situ-measured weed canopy (i.e., *Lolium* sp., *Echium* sp., and *Plantago* sp.), tree canopy (i.e., *Citrus sinensis* and *Citrus reticulata*), and bare soil spectra (i.e., Albic Luvisol [40]: sandy texture, organic carbon of 0.53%, and gravimetric moisture content θ ranging between 15% and 30%; Haplic Arenosol [40]: sandy texture, organic carbon of 1.91%, and θ ranging between 0% and 5%), measured in citrus orchards near Wellington, South Africa $(33°35'00''\mathrm{S}; 18°55'30''\mathrm{E})$, were used to generate simulated data. Simulated data are frequently used to evaluate analysis techniques since they inherently provide correct validation data [32], [33], [37]. Spectral measurements, approximately 100 for each cover class, were performed within 1 h of local solar noon on clear sky days using a full-range (350–2500 nm) spectroradiometer (ASD, Boulder, CO) with a 25° foreoptic. The spectroradiometer has a spectral resolution of 3 nm [full-width at half-maximum (FWHM)] and a 1.4-nm sampling interval across the 350–1050 nm spectral range. The FWHM and the sampling interval for the 1051–2500 nm spectral range are 20 and 2 nm, respectively. Resulting data were interpolated during collection by the ASD software to produce values at each nanometer interval. The reflectance data were calibrated using a white spectralon panel with nearly 100% reflectance at all wavelengths (Labsphere Inc., North Sutton, NH). Soil and weed canopy measurements were taken from nadir at a height of 1 m above the surface while tree canopy spectra were measured from nadir at 2 m above the tree top using a cherry picker. The major water absorption regions, sensitive to changing atmospheric water vapor content, were excluded, resulting in 1800 wavebands available for analysis.

Mixed spectra were calculated according to (1). Endmember combinations and subpixel cover fractions were randomly assigned to each pixel [21], [33]. The following three scenarios, each containing 10 000 simulated mixed pixel spectra, were

Authorized licensed use limited to: UNIVERSIDAD DE LA SERENA. Downloaded on October 26, 2009 at 07:46 from IEEE Xplore. Restrictions apply.

generated: 1) scenario I: a mixture of *C. sinensis* and *Lolium* sp.; 2) scenario II: a mixture of *C. sinensis*, *Echium* sp., and Arenosol soil; and 3) scenario III: a mixture of *C. reticulata*, *Plantago* sp., and Luvisol soil. In each scenario, a flat 1% reflectance spectrum was used as a surrogate for shading and shadowing effects [11], [14], [41]. In actual imagery, some of the image pixels will not contain all endmembers. Therefore, a set of 1000 mixtures was added to each scenario. The added mixtures were generated using the same approach as outlined above, yet, each time randomly excluding at least one of the endmembers.

Fig. 3 shows the presented variability (i.e., reflectance and derivatives) for each endmember class. The similarity between weed and tree spectra, as such, becomes evident.

B. Experimental Methodology

The performance of **InSU** to map the spatial distribution of weed patches in *Citrus* orchards was evaluated against the **LSMA** and **DSU** approaches. The abundance error (Δf) [33], the root mean square error (RMSE) [14], and the coefficient of determination (R^2), slope, and intercept of the estimated versus real (i.e., ground truth) cover fractions in a scatterplot were used to assess the subpixel weed cover classification accuracy [11]. The DSU approach was subdivided into the following: 1) $\mathbf{D^1SU}$, in which only first derivatives were used and 2) $\mathbf{D^2SU}$ in which only second derivatives were used. Higher order derivatives are more sensitive to high-frequency noise (see Section III-C) [37]. Therefore, the following two different InSU approaches were tested: 1) $\mathbf{InSU^{D1,R}}$, in which original reflectance spectra and first derivatives were integrated and second derivatives were excluded, and 2) $\mathbf{InSU^{D1,2,R}}$, in which reflectance, first and second derivatives spectra were integrated. Further, the LSMA, DSU, and InSU approaches were tested with ($\mathbf{LSMA}^*, \mathbf{DSU}^*, \mathbf{InSU}^*$) and without (**LSMA**, **DSU**, **InSU**) applying the feature selection algorithm summarized in Section II-D3. This allowed a proper and individual evaluation of the feature selection protocol and the integration of reflectance and derivative data.

C. Effects of Noise and Smoothing

It is common knowledge that derivative analysis greatly enhances high-frequency noise. Because of ambient and instrumental errors, this type of noise is inherent to hyperspectral data. As a result, the performances of DSU approaches (such as InSU) will depend on the signal-to-noise ratio (SNR) of the available spectral data [31], [37]. To determine the usefulness of InSU, it is essential to quantify its robustness against noise.

Therefore, noise was added to the simulated hyperspectral data sets described in Section III-A using a standard normal distribution of randomly generated numbers, i.e.,

$$r_{n,i} = r_i + \left(A \times \frac{e(0,1)}{\text{SNR}} \right) \tag{7}$$

where r is the reflectance at wavelength or spectral band i, e is a randomly generated number from a normal distribution with a mean of zero and a standard deviation of one [33], and A is the assumed reflectance for the spectrum. SNRs of $50:1$, $200:1$, and $500:1$ were used, assuming a 50% absolute reflectance (i.e., A). The selected range of SNRs was assumed appropriate to mimic the noise observed in hyperspectral images [33], [42].

Spectral smoothing preprocessing is a commonly accepted technique to (partly) circumvent the noise problem in derivative analysis. Prior to derivative analysis, a Savitzky–Golay smoothing filter (filter size $= 50$ wavebands) was therefore applied on the data [43], [44]. This approach is based on a simplified polynomial LS procedure. To further determine the usefulness of InSU, the combined effect of the smoothing filter size, the SNR, and the SMA accuracy was evaluated.

D. Simulated Airborne Visible Infrared Imaging Spectrometer (AVIRIS) Data

Most airborne and spaceborne sensors have fewer bands compared to ground-based spectroradiometers. In an additional simulation, the spectra from the ASD sensor were, therefore, resampled to match the wavebands of the AVIRIS data [45]. AVIRIS collects data in the spectral range of 400–2500 nm sampled by 224 spectral channels with a nominal 10 nm sampling [42]. Additionally, the 1998 AVIRIS waveband-specific SNR profile, reported by Green *et al.* [42], was introduced based on (7) to generate a typical AVIRS noise-degraded signal. These simulations allowed a more realistic evaluation of the robustness of InSU.

IV. Results

Fig. 4 summarizes Δf, RMSE, and R^2, slope, and intercept of the modeled versus observed weed cover fractions in a scatterplot for each of the tested SMA approaches. Results are shown for the different noise levels (SNR: no noise, $500:1$, $200:1$, $50:1$) as well as for the simulated AVIRIS data (Section III-C).

Despite being robust for ambient and instrumental noise, the **traditional LSMA** approach provided the least accurate weed cover fraction estimates ($\Delta f = [0.08, 0.17]$, $\text{RMSE} = [0.09, 0.16]$, $R^2 = [0.23, 0.32]$, $\text{slope} = [0.58, 0.96]$, and $\text{intercept} = [0.07, 0.11]$) in all scenarios and for all noise levels. Improvements were obtained when combining **derivative analysis** and LSMA (**DSU**; $\Delta f = [0.05, 0.12]$, $\Delta_{\Delta f} = \pm 0.05$; $\text{RMSE} = [0.07, 0.12]$, $\Delta\text{RMSE} = \pm 0.04$; $R^2 = [0.41, 0.72]$, $\Delta R^2 = \pm 0.25$; $\text{slope} = [0.58, 1]$, $\Delta\text{slope} = \pm 0.15$; $\text{intercept} = [0.02, 0.09]$, $\Delta\text{intercept} = \pm 0.03$). For noise-free data, no clear conclusions could be drawn regarding the relative performance of D^2SU compared to D^1SU (Fig. 4). However, overall, the observed decrease in accuracy with decreasing SNR was most pronounced for D^2SU (Fig. 4).

For SNRs $> 50:1$, the **integration of original reflectance and derivative endmember spectra** in a single analysis improved weed cover estimation in each scenario (InSU, Fig. 4) compared to LSMA. For most scenarios and noise levels, this was also true compared to DSU, except for some cases where the accuracies of DSU and InSU were the same (Fig. 4).

In scenarios I and III, the integration of the original reflectance and first- and second-order derivatives ($\mathbf{InSU^{D1,2,R}}$) was preferred over the integration of just the reflectance and

Authorized licensed use limited to: UNIVERSIDAD DE LA SERENA. Downloaded on October 26, 2009 at 07:46 from IEEE Xplore. Restrictions apply.

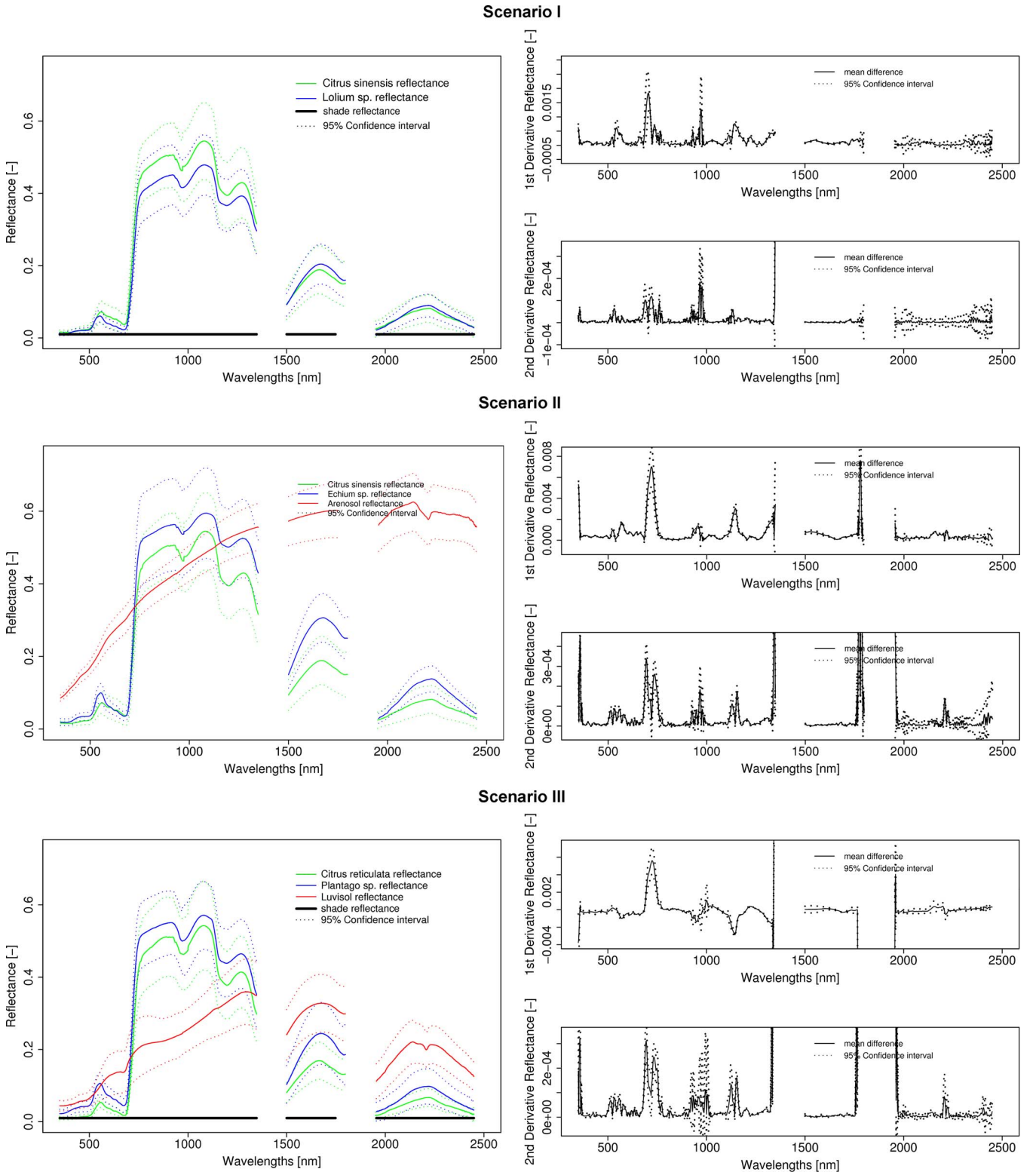

Fig. 3. (Top) Mean and 95% confidence interval of the original reflectance features for each endmember class; the mean difference in the (middle) first-derivative and (bottom) second-derivative spectra among the endmember classes. The 95% confidence intervals are also indicated.

first derivatives ($\mathbf{InSU^{D1,R}}$). In scenario II, both approaches provided similar accuracies (Fig. 4). For the simulated AVIRIS data, improvements in integrating magnitude- and shape-related information were observed for each scenario ($\Delta f = [0.04, 0.07]$, $\Delta_{\Delta f} = \pm 0.02$; RMSE $= [0.06, 0.08]$, ΔRMSE $= \pm 0.02$; $R^2 = [0.57, 0.72]$, $\Delta R^2 = \pm 0.07$; slope $= [0.80, 0.91]$, Δslope $= \pm 0.06$; intercept $= [0.03, 0.08]$, Δintercept $= \pm 0.01$), and overall, the accuracies of $\mathrm{InSU^{D1,2,R}}$ were higher than those of $\mathrm{InSU^{D1,R}}$, except for scenario II, in which both provided approximately the same results (Fig. 4).

Authorized licensed use limited to: UNIVERSIDAD DE LA SERENA. Downloaded on October 26, 2009 at 07:46 from IEEE Xplore. Restrictions apply.

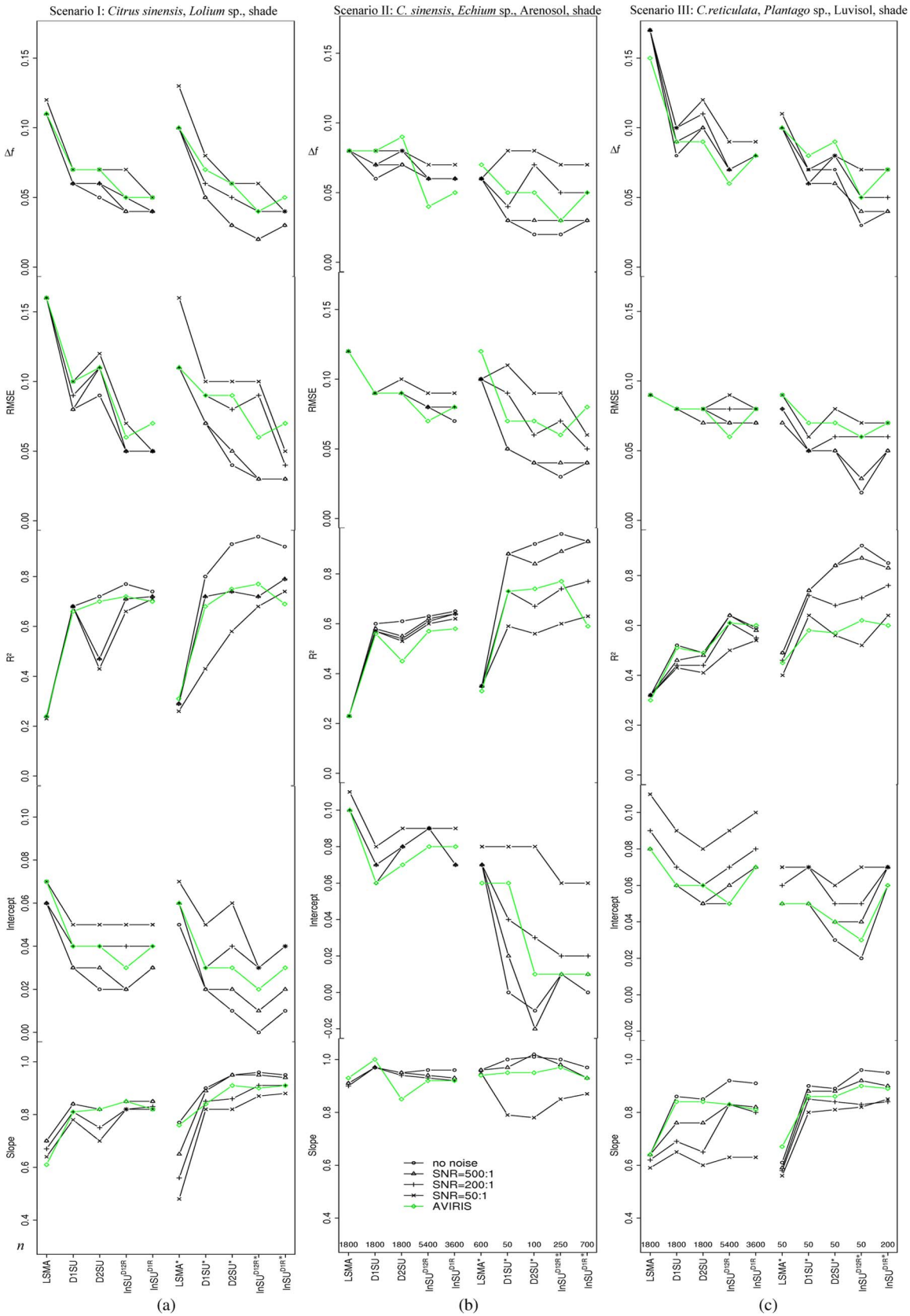

Fig. 4. Fraction abundance error (Δf), RMSE, the coefficient of determination (R^2), and slope and intercept of the modeled versus observed weed cover fractions in a scatterplot for different SMA approaches, different SNR levels (no noise, 500 : 1, 200 : 1, 50 : 1), and different scenarios. The SMA models that incorporate the waveband selection technique, as described in Section II-D3, are marked with an asterisk $(^*)$. At the bottom of the plots, the number of spectral features used in the mixture analysis (n) is shown. Results are also shown (in gray) for the simulated AVIRIS data (Section III-D). n should be divided by 10 to obtain the number of wavebands used in the analysis of the simulated AVIRIS data. (a) Scenario I: *C. sinensis*, *Lolium* sp., shade. (b) Scenario II: *C. sinensis*, *Echium* sp., Arenosol, shade. (c) Scenario III: *C. reticulata*, *Plantago* sp., Luvisol, shade.

Authorized licensed use limited to: UNIVERSIDAD DE LA SERENA. Downloaded on October 26, 2009 at 07:46 from IEEE Xplore. Restrictions apply.

The **automated ISI-driven feature selection algorithm** ($\mathbf{LSMA^*}$, $\mathbf{D^1SU^*}$, $\mathbf{D^2SU^*}$, $\mathbf{InSU^{D1,2,R^*}}$, $\mathbf{InSU^{D1,R^*}}$) was proposed to improve the separability between weed and tree spectra (Section II-D3; Fig. 2). Compared to the traditional approaches using all wavebands ($\Delta f = [0.04, 0.17]$, RMSE $= [0.05, 0.16]$, $R^2 = [0.22, 0.78]$, slope $= [0.58, 1.02]$, and intercept $= [0.02, 0.11]$), the implementation of the feature selection algorithm ($\Delta f = [0.02, 0.13]$, RMSE $= [0.01, 0.13]$, $R^2 = [0.29, 0.96]$, slope $= [0.45, 1.02]$, and intercept $= [-0.02, 0.08]$) resulted in an average increase of ± 0.18 in R^2 and decrease of ± 0.03 and ± 0.02 in Δf and RMSE, respectively (Fig. 4).

For the noise-free data, the highest accuracies were achieved for $\text{InSU}^{\text{D1,2,R}^*}$ compared with the results of LSMA^*, D^1SU^*, D^2SU^*, and $\text{InSU}^{\text{D1,R}^*}$ (Fig. 4). However, with decreasing SNRs, there was a shift toward $\text{InSU}^{\text{D1,R}^*}$. Yet, for the simulated AVIRIS data, the overall highest accuracy in each scenario was obtained for the $\text{InSU}^{\text{D1,2,R}^*}$ ($\Delta f = [0.03, 0.05]$, RMSE $= 0.06$, $R^2 = [0.62, 0.77]$, slope $= [0.85, 0.95]$, and intercept $= [0.01, 0.03]$).

For each scenario, the spectral features selected for use in $\text{InSU}^{\text{D1,2,R}^*}$ and $\text{InSU}^{\text{D1,R}^*}$ are highlighted as black and gray dots, respectively, at the bottom of Fig. 5. The number and type of wavebands or spectral features selected by the automated ISI-driven feature selection algorithm depend on the considered scenario and the available spectral information (Fig. 5). According to Somers *et al.* [34], wavebands were selected in groups of 50. For the **first scenario**, which is a mixture of weed, tree canopy, and shade spectra, the 100 most stable spectral features (lowest ISI) were selected by $\text{InSU}^{\text{D1,2,R}^*}$. All of the selected features were shape related because both first and second derivatives were included. The original reflectance spectra, as such, did not contribute and could as well have been discarded. The selected wavebands were spread over the 500–1700 nm domain, and the analysis resulted in improvements over the traditional DSU and LSMA approaches (Fig. 4). If no second derivatives were used ($\text{InSU}^{\text{D1,R}^*}$), the number of selected features increased to 150. Most of them were first derivatives, yet, 20 wavebands (around 680 nm) were selected from the original reflectance spectra, resulting in an increase in weed cover estimate accuracy over D^1SU^* and LSMA^* (Fig. 4). Despite the presence of a soil component, similar weed cover estimate accuracies were achieved for scenarios II and III (Fig. 4). In the **second scenario**, 250 wavebands were selected for use in $\text{InSU}^{\text{D1,2,R}^*}$. Again, only shape-related spectral features, spread over the 450–1600 nm domain, were used. $\text{InSU}^{\text{D1,R}^*}$ selected 700 wavebands, most of them first derivatives. However, approximately 150 wavebands were selected from the original reflectance in the SWIR2 (2050–2400 nm), resulting in an increase in weed cover estimate accuracy compared to D^1SU^* and LSMA^* (Fig. 4). In the **third scenario**, only 50 wavebands were used by $\text{InSU}^{\text{D1,2,R}^*}$. Yet, the selected subset contained both original and first- and second-derivative reflectance features, most of them from the visible (VIS: 350–700 nm) domain. For $\text{InSU}^{\text{D1,R}^*}$, the number of stable features increased to 200. The 90 bands selected from the original reflectance spectra were mainly centered at 520 nm.

Fig. 6 assesses the robustness of $\text{InSU}^{\text{D1,2,R}^*}$ and $\text{InSU}^{\text{D1,R}^*}$ against ambient or instrumental **noise**. The combined effect of the SNR, the smoothing filter size, and the SMA accuracy

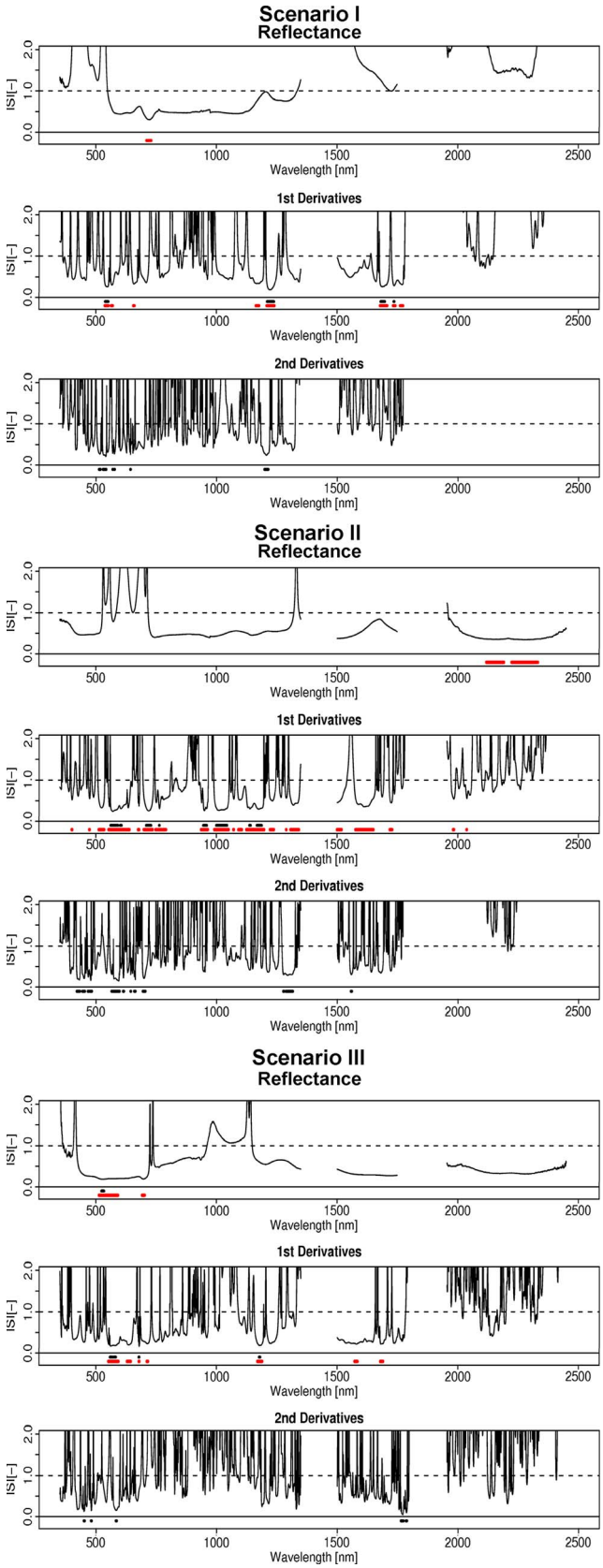

Fig. 5. ISI plotted against wavelength for each scenario. Results are shown for the (top) original reflectance spectra and the (middle) first-derivative and (bottom) second-derivative spectra. The features selected by the $\text{InSU}^{\text{D1,2,R}^*}$ and $\text{InSU}^{\text{D1,R}^*}$ approaches are highlighted as black and gray dots at the bottom of the plots, respectively.

Authorized licensed use limited to: UNIVERSIDAD DE LA SERENA. Downloaded on October 26, 2009 at 07:46 from IEEE Xplore. Restrictions apply.

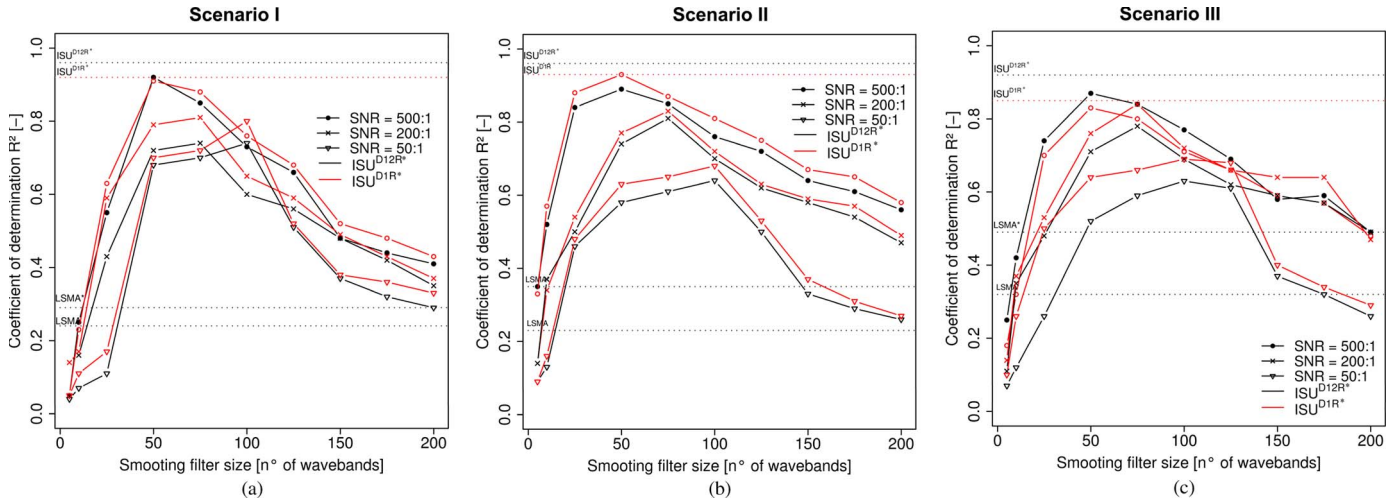

Fig. 6. Combined effect of smoothing filter size, SNR, and the coefficient of determination (R^2) of the $\text{InSU}^{\text{D1,2,R}^*}$ and $\text{InSU}^{\text{D1,R}^*}$ approaches estimated versus real weed cover fractions. The dotted horizontal lines indicate the accuracy levels (R^2) for LSMA, LSMA*, $\text{InSU}^{\text{D1,2,R}^*}$, and $\text{InSU}^{\text{D1,R}^*}$ as applied on noise-free data (Table I). (a) Scenario I. (b) Scenario II. (c) Scenario III.

is shown. From Fig. 4, it was already clear that the accuracy of InSU* dropped as the SNR decreased, and that this drop was more pronounced for the $\text{InSU}^{\text{D1,2,R}^*}$. By increasing the **smoothing filter size**, the accuracy clearly increased. A critical point was reached after which SMA accuracy drops again (Fig. 6). These points were similar for all scenarios but shifted toward larger filter sizes when the SNR decreased. The following general conclusions valid for the three investigated scenarios could be drawn.

1) For a SNR of 500 : 1, the optimal filter size was 50 wavebands, and the average accuracy for $\text{InSU}^{\text{D1,R}^*}$ and $\text{InSU}^{\text{D1,2,R}^*}$ are, respectively, $\Delta f = (0.04, 0.03)$, RMSE$= (0.05, 0.04)$, $R^2 = (0.88, 0.89)$, slope $= (0.92, 0.95)$, and intercept $= (0.03, 0.02)$.
2) For a SNR of 200 : 1, the optimal filter size was 75 wavebands, and the average accuracy for $\text{InSU}^{\text{D1,R}^*}$ and $\text{InSU}^{\text{D1,2,R}^*}$ are, respectively, $\Delta f = (0.06, 0.07)$, RMSE $= (0.06, 0.07)$, $R^2 = (0.83, 0.77)$, slope $= (0.91, 0.88)$, and intercept $= (0.04, 0.03)$.
3) For a SNR of 50 : 1, the optimal filter size was 100 wavebands, and the average accuracy for $\text{InSU}^{\text{D1,R}^*}$ and $\text{InSU}^{\text{D1,2,R}^*}$ are, respectively, $\Delta f = (0.08, 0.10)$, RMSE $= (0.07, 0.08)$, $R^2 = (0.70, 0.65)$, slope$= (0.84, 0.82)$, and intercept $= 0.06$.
4) For filter sizes ranging between 25 and 175 wavebands, and SNRs of 500 : 1 and 200 : 1, InSU* provided the most appropriate weed cover fraction estimates compared to all other tested LSMA approaches (Figs. 4 and 6). A tendency toward first derivatives $(\text{InSU}^{\text{D1,R}^*})$ was observed for higher noise levels.

V. Discussion

For all scenarios and all noise levels, the **traditional LSMA** approach provided the least accurate weed cover fraction estimates (see Fig. 4). As commonly accepted, this is explained by the high similarity between weed and tree spectra, evident from Fig. 3, resulting in unstable model inversion (e.g., [2], [12]–[14], [19], [37], and [38]).

The intraclass and interclass endmember variability was quantified using ISI [see (6)], and results are plotted in Fig. 5. A comparison between Figs. 3 and 5 shows that the wavebands or spectral features with high ISI values (Fig. 5) correspond to spectral features displaying a high similarity between, and/or a high variability within, endmember classes (Fig. 3). The opposite is true for low values. Lower ISI values for the derivatives (Fig. 5), therefore, illustrates that **derivative analysis (DSU)** resulted in a reduced similarity among the endmember classes compared to analysis of the original reflectance data, which, in its own, explains the improved weed cover estimates using the DSU approaches (Fig. 4). Debba *et al.* [37] also demonstrated lower correlation coefficients for pairs of derivatives compared to the original spectra of iron-bearing oxide, hydroxide, and sulfate minerals. Moreover, improved estimates of abundance of the spectrally similar minerals were shown for DSU compared to LSMA. Nevertheless, a decreased accuracy with decreasing SNR was observed for the DSU approaches, and the decrease was more pronounced for the D^{2}SU (Fig. 4). These results corroborate those of Debba *et al.* [37], who also found that for a SNR of approximately 50 : 1, the use of first derivatives in DSU was preferred over the use of second derivatives, while the opposite was true for noise-free data.

The **automated ISI-driven feature selection algorithm** was included in the mixture analysis $(\text{LSMA}^*, \text{D}^1\text{SU}^*, \text{D}^2\text{SU}^*)$ (Section II-D3; Fig. 2) to further improve the results of DSU. For a SNR up to 200 : 1, clear improvements over the traditional approaches using all wavebands were observed (Fig. 4). These improvements corroborate the results of [34] and reinforce the basic assumption that subpixel fraction estimates can be improved considerably by focusing on a subset of "stable" spectral features [8], [10], [34]. Overall, for the noise-free data, the highest accuracies were achieved for the second derivatives (D^2SU^*), while for SNRs $< 200 : 1$, the highest accuracies were observed for the first derivatives (D^1SU^*) (compare results of LSMA*, D^{1}SU*, and D^{2}SU* in Fig. 4). In [31], a similar

Authorized licensed use limited to: UNIVERSIDAD DE LA SERENA. Downloaded on October 26, 2009 at 07:46 from IEEE Xplore. Restrictions apply.

approach using second derivatives was successfully tested to map the distribution of rock-encrusting lichen communities. These authors, however, manually selected wavelengths to optimize the separability among endmembers. The relevance of the current results, therefore, is not only situated in validating the approach and highlighting the potential of using derivative spectra in mixture analysis. This study provides an additional improvement to the algorithm by adding an automated protocol for wavelength selection.

Further improvements in weed cover estimates using SMA were obtained by **integration of original reflectance and derivative data** in a single unmixing analysis ($\mathbf{InSU}$) (Fig. 4). For noise-free data, the integration of original and first- and second-derivative data ($\mathrm{InSU}^{\mathrm{D1,2,R}}$) was preferred. Yet, for SNRs of $200:1$ or higher, the gain of including second derivatives in the analysis decreased, and $\mathrm{InSU}^{\mathrm{D1},R}$ performed better. As previously reported, higher order derivatives are more sensitive to high-frequency noise compared to lower order derivatives [37].

Similar to LSMA and DSU, the performance of **InSU was further improved by including the automated ISI-driven feature selection algorithm** ($\mathbf{InSU}^{*}$) (Fig. 4). The number, type, and position of the selected wavelengths differed among scenarios and depended on the available spectral information (Fig. 5). Nevertheless, most of the selected wavebands were extracted from the VIS (350–700 nm) and near-infrared (NIR: 750–1050 nm) domain, indicating an improved separability among the endmembers in this spectral domain (Fig. 5). This corresponds to the results of previous studies [10], [36], [46] and could in the VIS domain be explained by slight changes in pigment concentration between both vegetation types caused by species-specific characteristics or unbalanced nutrient supplies [34]. These results further indicate that despite the presence of a dry (scenario II) or relatively wet (scenario III) soil component, the VIS and NIR domains are critical in extracting proper information on the subpixel distribution of weed patches. This contradicts the results reported by Asner and Lobell [8], who identified the SWIR2 (2050–2500 nm) region to be most appropriate to discriminate between soil and vegetation. The use of derivatives and the presence of similar vegetation types in addition to a soil component, as such, invalidate this assumption and make the VIS and NIR domains more appropriate for separation of the vegetation endmembers. Additional experiments with mixtures of different vegetation and soil types are, however, required to generalize this assumption.

As demonstrated in Figs. 4 and 6, derivative analysis and, as such, InSU and InSU^{*}, suffers from ambient and instrumental **noise**. Thus, proper smoothing operations are critical. As expected, without additional preprocessing (no or minor smoothing) InSU failed to provide acceptable weed cover fraction estimates for all noise levels (Fig. 6). By increasing the **smoothing filter** size, the accuracy clearly increased and eventually reaches a critical point after which SMA accuracy drops again (Fig. 6). The subsequent drop in accuracy is explained by the loss of spectral details in derivative spectra when the smoothing filter window exceeded a certain size [32]. The critical points were similar for all scenarios but shifted toward greater filter sizes when the SNR decreased. Overall, for filter sizes > 25, and a SNR of $200:1$ or better, InSU^{*} provided the most appropriate weed cover fraction estimates in all scenarios (Figs. 4 and 6). All DSU approaches suffered from noise effects similar to InSU and a tendency toward improved accuracies for the first derivatives, compared to the second derivatives, was observed (Fig. 4). Whether or not to use higher order derivatives in InSU is, as such, highly dependent on the quality of the spectral data. Smoothing filters can to some extent circumvent noise problems in DSU and InSU.

The robustness of InSU was further evaluated based on **simulated AVIRIS data**. The spectral bands of the ASD sensor were resampled, and typical AVIRIS noise degraded signals were generated (Section III-C). Model comparison (Fig. 4) showed that in general, similar conclusions could be drawn for the simulated AVIRIS data compared to the previous simulations performed in this study. Compared to the traditional LSMA and DSU approaches, improvements in weed cover estimates were achieved by 1) applying the automated ISI-driven feature selection algorithm and 2) integrating the original and derivative reflectance data. For all scenarios, the $\mathrm{InSU}^{\mathrm{D1,2,R}^{*}}$, integrating both original and first- and second-derivative spectra in an automated waveband selection protocol, provided the best results. A smoothing filter of ten AVIRIS wavebands, which corresponds to approximately 50 ASD wavebands, was used prior to analysis. Still, the results of $\mathrm{InSU}^{\mathrm{D1,2,R}^{*}}$ are prone to noise effects. It should, however, be recalled that, as is the case for AVIRIS [42], waveband-specific SNR profiles are available for most commonly used airborne and spaceborne sensors. Therefore, we propose to incorporate this information in the InSU approach as an additional criterion for waveband selection. From the analysis in Fig. 4, it was clear that for SNRs $< 200:1$, the accuracy of InSU dropped drastically. Therefore, AVIRIS wavebands with a SNR below this threshold were excluded from analysis. Subsequently, the remaining wavebands were exploited for derivative analysis and were included in the feature selection protocol as described in Section II-D-3. Results demonstrated that the accuracy of $\mathrm{InSU}^{\mathrm{D1,2,R}^{*}}$ in scenarios I, II, and III significantly increased to $R^2_{[\mathrm{I,II,III}]} = [0.81, 0.89, 0.67]$, $\mathrm{RMSE}_{[\mathrm{I,II,III}]} = [0.05, 0.04, 0.04]$, $\Delta f_{[\mathrm{I,II,III}]} = [0.03, 0.03, 0.04]$, $\mathrm{slope}_{[\mathrm{I,II,III}]} = [0.89, 0.96, 0.86]$, and $\mathrm{intercept}_{[\mathrm{I,II,III}]} = [0.02, 0.01, 0.02]$. These results are promising, although continued research should validate and optimize this approach on actual imagery. Taking these observations into mind, it can be concluded that InSU^{*}, although sensitive to noise, provides an interesting tool for a dynamic and accurate site-specific weed patch monitoring. Complementary information is provided by integration of different shape-related (i.e., first and second derivatives) and magnitude-related spectral features, while maximum separability between endmembers is achieved by selecting stable features (low ISI). However, the nature and amount of features to provide optimal weed cover fraction estimates clearly depend on the spectral characteristics of the presented endmembers (species composition, age class, biophysical, and biochemical status, etc.). For the first scenario, all of the selected features were shape related because both first and second derivatives were included in the InSU^{*} analysis (Fig. 5). The original reflectance spectra, as such, did not contribute and could as well have been discarded. However, this is not always the case. In scenario III for example, original reflectance features as well as first- and

Authorized licensed use limited to: UNIVERSIDAD DE LA SERENA. Downloaded on October 26, 2009 at 07:46 from IEEE Xplore. Restrictions apply.

TABLE I
COEFFICIENT OF DETERMINATION (R^2) AND THE SLOPE AND INTERCEPT OF THE MODELED VERSUS OBSERVED WEED COVER FRACTIONS FOR DIFFERENT SMA APPROACHES AND DIFFERENT SCENARIOS. THE SMA APPROACHES WERE EVALUATED USING ALL THE AVAILABLE ENDMEMBER SPECTRA (100%) AND A RANDOM SELECTION OF 50% AND 25% OF THE AVAILABLE SPECTRA, RESPECTIVELY. RESULTS ARE SHOWN FOR THE DATA WITH A SNR OF 500 : 1

Scenario		R^2*			Intercept*			Slope*		
		100%	50%	25%	100%	50%	25%	100%	50%	25%
I	LSMA	0.24	0.24	0.18	0.06	0.06	0.06	0.70	0.67	0.66
	D^1SU	0.68	0.65	0.46	0.03	0.06	0.09	0.84	0.82	0.79
	D^2SU	0.48	0.41	0.29	0.03	0.06	0.06	0.82	0.81	0.80
	$InSU^{D1,2,R}$	0.74	0.65	0.40	0.02	0.04	0.04	0.85	0.84	0.84
	$InSU^{D1,R}$	0.72	0.62	0.45	0.03	0.05	0.05	0.85	0.83	0.80
	LSMA*	0.29	0.26	0.20	0.06	0.07	0.08	0.65	0.63	0.57
	D^1SU^*	0.80	0.74	0.56	0.02	0.04	0.05	0.89	0.87	0.87
	D^2SU^*	0.90	0.79	0.61	0.02	0.03	0.04	0.95	0.93	0.91
	$InSU^{D1,2R*}$	0.92	0.78	0.64	0.01	0.02	0.02	0.95	0.95	0.93
	$InSU^{D1,R*}$	0.91	0.71	0.64	0.02	0.03	0.04	0.94	0.93	0.92
II	LSMA	0.23	0.23	0.20	0.10	0.10	0.12	0.91	0.90	0.88
	D^1SU	0.58	0.53	0.43	0.07	0.07	0.07	0.97	0.94	0.83
	D^2SU	0.55	0.47	0.36	0.08	0.08	0.08	0.95	0.93	0.86
	$InSU^{D1,2,R}$	0.62	0.56	0.46	0.09	0.10	0.10	0.94	0.90	0.87
	$InSU^{D1,R}$	0.64	0.57	0.47	0.07	0.07	0.07	0.93	0.90	0.86
	LSMA*	0.35	0.35	0.25	0.07	0.10	0.14	0.96	0.76	0.68
	D^1SU^*	0.88	0.83	0.67	0.02	0.03	0.03	0.97	0.93	0.90
	D^2SU^*	0.84	0.77	0.66	-0.02	0.03	0.04	1.02	0.96	0.89
	$InSU^{D1,2,R*}$	0.89	0.80	0.67	0.01	0.02	0.04	0.98	0.97	0.95
	$InSU^{D1,R*}$	0.93	0.88	0.75	0.01	0.02	0.02	0.93	0.93	0.91
III	LSMA	0.32	0.32	0.30	0.08	0.08	0.08	0.64	0.64	0.61
	D^1SU	0.46	0.45	0.42	0.06	0.09	0.11	0.76	0.75	0.73
	D^2SU	0.48	0.42	0.34	0.05	0.06	0.07	0.76	0.75	0.72
	$InSU^{D1,2,R}$	0.64	0.62	0.52	0.06	0.08	0.11	0.83	0.78	0.77
	$InSU^{D1,R}$	0.58	0.53	0.45	0.07	0.09	0.12	0.82	0.76	0.76
	LSMA*	0.49	0.43	0.39	0.05	0.06	0.06	0.59	0.56	0.56
	D^1SU^*	0.74	0.71	0.61	0.05	0.06	0.07	0.88	0.85	0.81
	D^2SU^*	0.84	0.83	0.72	0.04	0.04	0.05	0.88	0.87	0.83
	$InSU^{D1,2,R*}$	0.87	0.83	0.78	0.04	0.04	0.05	0.92	0.88	0.87
	$InSU^{D1,R*}$	0.83	0.81	0.73	0.07	0.08	0.08	0.90	0.85	0.84

* results show the average values for 100 random iterations

second-order derivatives were selected in the optimal spectral subset. Decisions on whether to exclude original or derivative spectra from the analysis are therefore difficult to make manually as this is case sensitive and prone to the spectral characteristics of the presented endmembers. Despite this, the automated ISI-driven feature selection algorithm allows $InSU^*$ to automatically adapt to the spectral characteristics of the presented endmembers and allows, in variable situations, selecting the optimal set of spectral features (original or derivative reflectance) for accurate fraction estimates. This is specifically important for weed detection as spectral discrimination efficiency of weeds and crops is consistently affected by consecutive phenological developmental stages [47]. Important to highlight is that similar to most LSMA approaches, an appropriate spectral endmember library is vital for a proper functioning of the technique (e.g., [7], [8], [11], [14], [20], and [30]). Results in Table I show an overall drop in R^2, between the modeled and observed weed cover fractions, as the spectral endmember library size decreases. Similar conclusions could be drawn for the slope and intercept (Fig. 4). The ISI-driven spectral feature selection algorithm requires proper information on the intraclass variability. A detailed statistical analysis on the minimum or optimal library size in relation to the presented intraclass variability is required. In this light, continued research should focus on validating the approach using actual imagery and spectral libraries built from automated endmember selection techniques such as those proposed in [21] and [26]. In particular, the technique described in [26] is interesting as it allows constructing endmember bundles from image data expressing as such the intraclass endmember variability. Alternatively, lookup tables [48] linking phenological development stages and the spectral variability of weed and crop canopies could be used. Such an approach, however, requires an extensive set of reliable field measurements.

Authorized licensed use limited to: UNIVERSIDAD DE LA SERENA. Downloaded on October 26, 2009 at 07:46 from IEEE Xplore. Restrictions apply.

VI. Conclusion

This study has successfully tested an alternative SMA approach that allows for the discrimination between weed and crop canopy spectra. General traditional approaches fail to do so because of the high spectral similarity among the different vegetation types. The approach presented in this paper, referred to as InSU, combines both shape (first and second derivatives)- and magnitude (original reflectance)-related spectral features in an automated waveband selection protocol. Analysis of simulated mixtures of *in situ*-measured *Citrus* canopy, weed canopy, and soil spectra markedly illustrated improved weed cover fraction estimates for InSU over traditional approaches. The added value of incorporating derivative analysis in LSMA, as such, was demonstrated. Consistent results were observed for different scenarios, highlighting that InSU provides a powerful tool as a dynamic weed development monitoring technique. Although the algorithm needs validation in field situations (e.g., to address the influence of nonlinear mixing effects and imagery-specific SNRs) [49], a promising tool is presented that might also be relevant in other ecosystems or application domains in which highly similar endmembers need to be separated.

Acknowledgment

The authors would like to thank the Faculty of Agriculture, University of Stellenbosch, South Africa, for logistic support to collect *in situ* data for this study.

References

[1] M. Kunisch, "Precision farming, a tool for weed control?" *J. Plant Dis. Protection*, vol. 18, pp. 415–420, 2002.

[2] D. W. Lamb and R. B. Brown, "Remote-sensing and mapping of weeds in crops," *J. Agric. Eng. Res.*, vol. 78, no. 2, pp. 117–125, Feb. 2001.

[3] K. R. Thorp and L. F. Thian, "A review on remote sensing of weeds in agriculture," *Precision Agric.*, vol. 5, no. 5, pp. 477–508, Oct. 2004.

[4] M. S. Moran, Y. Inoue, and E. M. Barnes, "Opportunities and limitations for image-based remote sensing in precision crop management," *Remote Sens. Environ.*, vol. 61, no. 3, pp. 319–346, Sep. 1997.

[5] P. K. Goel, S. O. Prasher, J. A. Landry, R. M. Patel, and A. A. Viau, "Hyperspectral image classification to detect weed infestations and nitrogen status in corn," *Trans. ASAE*, vol. 46, no. 2, pp. 539–550, 2003.

[6] J. B. Adams, M. O. Smith, and A. R. Gillespie, "Imaging spectroscopy: Interpretation based on spectral mixture analysis," in *Remote Geochemical Analysis: Elemental and Mineralogical Composition 7*, C. M. Pieters and P. Englert, Eds. New York: Cambridge Univ. Press, 1993, pp. 145–166.

[7] D. A. Roberts, M. Gardner, R. Church, S. Ustin, G. Scheer, and R. O. Green, "Mapping Chaparral in the Santa Monica Mountains using multiple endmembers spectral mixture models," *Remote Sens. Environ.*, vol. 65, no. 3, pp. 267–279, Sep. 1998.

[8] G. P. Asner and D. B. Lobell, "A biogeophysical approach for automated SWIR unmixing of soils and vegetation," *Remote Sens. Environ.*, vol. 74, no. 1, pp. 99–112, Oct. 2000.

[9] D. R. Peddle and A. M. Smith, "Spectral mixture analysis of agricultural crops: Endmember validation and biophysical estimation in potato plots," *Int. J. Remote Sens.*, vol. 26, no. 22, pp. 4959–4979, Jan. 2005.

[10] X. Miao, P. Gong, S. Swope, R. Pu, R. Carruthers, G. L. Anderson, J. S. Heaton, and C. R. Tracy, "Estimation of yellow starthistle abundance through CASI-2 hyperspectral imagery using linear spectral mixture models," *Remote Sens. Environ.*, vol. 101, no. 3, pp. 329–341, Apr. 2006.

[11] B. Somers, S. Delalieux, W. W. Verstraeten, and P. Coppin, "A conceptual framework for the simultaneous extraction of sub-pixel spatial extent and spectral characteristics of crops," *Photogramm. Eng. Remote Sens.*, vol. 75, no. 1, pp. 57–68, 2009.

[12] G. S. Okin, D. A. Roberts, B. Murray, and W. J. Okin, "Practical limits on hyperspectral vegetation discrimination in arid and semiarid environments," *Remote Sens. Environ.*, vol. 77, no. 2, pp. 212–225, Aug. 2001.

[13] J. Settle, "On the effect of variable endmember spectra in the linear mixture model," *IEEE Trans. Geosci. Remote Sens.*, vol. 44, no. 2, pp. 389–396, Feb. 2006.

[14] B. Somers, S. Delalieux, J. Stuckens, W. W. Verstraeten, and P. Coppin, "A weighted linear spectral mixture analysis approach to address endmember variability in agricultural production systems," *Int. J. Remote Sens.*, vol. 30, no. 1, pp. 139–147, Jan. 2009.

[15] G. J. Fitzgerald, P. J. Pinter, D. J. Hunsaker, and T. R. Clarke, "Multiple shadow fractions in spectral mixture analysis of cotton canopy," *Remote Sens. Environ.*, vol. 97, no. 4, pp. 526–539, Sep. 2005.

[16] D. A. Roberts, "Separating spectral mixtures of vegetation and soil," Ph.D. dissertation, Univ. Washington, Seattle, WA, 1991.

[17] C. C. Borel and S. A. Gerstl, "Nonlinear spectral mixing models for vegetative and soil surfaces," *Remote Sens. Environ.*, vol. 47, no. 3, pp. 403–416, Mar. 1994.

[18] Y. Gu, Y. Zhang, and J. Zhang, "Integration of spatial–spectral information for resolution enhancement in hyperspectral images," *IEEE Trans. Geosci. Remote Sens.*, vol. 46, no. 5, pp. 1347–1358, May 2008.

[19] A. Barducci and A. Mecocci, "Theoretical and experimental assessment of noise effects on least-squares spectral unmixing of hyperspectral images," *Opt. Eng.*, vol. 44, no. 8, pp. 087 008.1–087 008.17, Aug. 2005.

[20] S. Tompkins, J. F. Mustard, C. M. Pieters, and D. W. Forsyth, "Optimization of endmembers for spectral mixture analysis," *Remote Sens. Environ.*, vol. 59, no. 3, pp. 472–489, Mar. 1997.

[21] A. Plaza, P. Martinez, R. Perez, and J. Plaza, "A quantitative and comparative analysis of endmember extraction algorithms from hyperspectral data," *IEEE Trans. Geosci. Remote Sens.*, vol. 42, no. 3, pp. 650–663, Mar. 2004.

[22] L. Miao and H. Qi, "Endmember extraction from highly mixed data using minimum volume constrained nonnegative matrix factorization," *IEEE Trans. Geosci. Remote Sens.*, vol. 45, no. 3, pp. 765–777, Mar. 2007.

[23] J. Wang and C.-I Chang, "Applications of independent component analysis in endmember extraction and abundance quantification for hyperspectral imagery," *IEEE Trans. Geosci. Remote Sens.*, vol. 44, no. 9, pp. 2601–2616, Sep. 2006.

[24] A. Plaza and C.-I Chang, "Impact of initialization on design of endmember extraction algorithms," *IEEE Trans. Geosci. Remote Sens.*, vol. 44, no. 11, pp. 3397–3407, Nov. 2006.

[25] M. A. Theseira, G. Thomas, J. C. Taylor, F. Gemmell, and J. Varjo, "Sensitivity of mixture modelling to end-member selection," *Int. J. Remote Sens.*, vol. 24, no. 7, pp. 1559–1575, Apr. 2003.

[26] C. A. Bateson, G. P. Asner, and C. A. Wessman, "Endmember bundles: A new approach to incorporating endmember variability into spectral mixture analysis," *IEEE Trans. Geosci. Remote Sens.*, vol. 38, no. 2, pp. 1083–1094, Mar. 2000.

[27] C. Hecker, M. van der Meijde, H. van der Werff, and F. D. van der Meer, "Assessing the influence of reference spectra on synthetic SAM classification results," *IEEE Trans. Geosci. Remote Sens.*, vol. 46, no. 12, pp. 4162–4172, Dec. 2008.

[28] J. B. Adams, D. Sabol, V. Kapos, R. A. Filho, D. A. Roberts, M. O. Smith, and A. R. Gillespie, "Classification of multispectral images based on fractions of endmembers: Application to land-cover change in the Brazilian Amazon," *Remote Sens. Environ.*, vol. 52, no. 2, pp. 137–154, May 1995.

[29] J. Li, "Wavelet-based feature extraction for improved endmember abundance estimation in linear unmixing of hyperspectral signals," *IEEE Trans. Geosci. Remote Sens.*, vol. 42, no. 3, pp. 644–649, Mar. 2004.

[30] C. Wu, "Normalized spectral mixture analysis for monitoring urban composition using ETM$^+$ imagery," *Remote Sens. Environ.*, vol. 93, no. 4, pp. 480–492, Dec. 2004.

[31] J. Zhang, B. Rivard, and A. Sanchez-Azofeifa, "Derivative spectral unmixing of hyperspectral data applied to mixtures of lichen and rock," *IEEE Trans. Geosci. Remote Sens.*, vol. 42, no. 9, pp. 1934–1940, Sep. 2004.

[32] C. Song, "Spectral mixture analysis for subpixel vegetation fractions in the urban environment: How to incorporate endmember variability?" *Remote Sens. Environ.*, vol. 95, no. 2, pp. 248–263, Mar. 2005.

[33] D. M. Rogge, B. Rivard, J. Zhang, and J. Feng, "Iterative spectral unmixing for optimizing per-pixel endmember sets," *IEEE Trans. Geosci. Remote Sens.*, vol. 44, no. 12, pp. 3725–3736, Dec. 2006.

[34] B. Somers, S. Delalieux, W. W. Verstraeten, J. A. N. van Aardt, G. L. Albrigo, and P. Coppin, "An automated waveband selection technique for optimized hyperspectral mixture analysis," *Int. J. Remote Sens.* to be published.

[35] J. Zhang, B. Rivard, A. Sanchez-Azofeifa, and K. Castro-Esau, "Intra- and inter-class spectral variability of tropical tree species at La Selva Costa Rica: Implications for species identification using HYDICE imagery," *Remote Sens. Environ.*, vol. 105, no. 2, pp. 129–141, Nov. 2006.

Authorized licensed use limited to: UNIVERSIDAD DE LA SERENA. Downloaded on October 26, 2009 at 07:46 from IEEE Xplore. Restrictions apply.

[36] J. A. N. van Aardt and R. H. Wynne, "Spectral separability among six southern tree species," *Photogramm. Eng. Remote Sens.*, vol. 67, no. 12, pp. 1367–1375, 2001.
[37] P. Debba, E. J. M. Carranza, F. D. van der Meer, and A. Stein, "Abundance estimation of spectrally similar minerals by using derivative spectra in simulated annealing," *IEEE Trans. Geosci. Remote Sens.*, vol. 44, no. 12, pp. 3649–3658, Dec. 2006.
[38] F. Van der Meer and S. M. De Jong, "Improving results of spectral unmixing of Landsat Thematic Mapper imagery by enhancing the orthogonality of end-members," *Int. J. Remote Sens.*, vol. 21, no. 15, pp. 2781–2797, Oct. 2000.
[39] R. L. Pu, P. Gong, G. S. Biging, and M. R. Larrieu, "Extraction of red edge optical parameters from Hyperion data for estimation of forest leaf area index," *IEEE Trans. Geosci. Remote Sens.*, vol. 41, no. 4, pp. 916–921, Apr. 2003.
[40] FAO, *FAO world reference base for soil resources*, 1998, Rome, Italy: Food Agric. Org. United Nations.
[41] C. C. D. Lelong, P. C. Pinet, and H. Poilvé, "Hyperspectral imaging and stress mapping in agriculture: A case study on wheat in Beauce (France)," *Remote Sens. Environ.*, vol. 66, no. 2, pp. 179–191, Nov. 1998.
[42] R. Green, B. Pavri, J. Faust, and O. Williams, "AVIRIS radiometric laboratory calibration in flight validation and a focused sensitivity analysis in 1998," in *Proc. AVIRIS Workshop*, Pasadena, CA, 1999, pp. 161–176.
[43] A. Savitzky and M. J. Golay, "Smoothing and differentiation of data by simplified least squares procedures," *Anal. Chem.*, vol. 36, no. 8, pp. 1627–1639, Jul. 1964.
[44] P. J. Zarco-Tejada, J. R. Miller, G. H. Mohammed, T. L. Noland, and P. H. Sampson, "Scaling-up and model inversion methods with narrowband optical indices for chlorophyll content estimation in closed forest canopies with hyperspectral data," *IEEE Trans. Geosci. Remote Sens.*, vol. 39, no. 7, pp. 1491–1507, Jul. 2001.
[45] A. P. Williams and E. R. Hunt, Jr., "Estimation of leafy spurge cover from hyperspectral imagery using mixture tuned matched filtering," *Remote Sens. Environ.*, vol. 82, no. 2/3, pp. 446–456, Oct. 2002.
[46] R. Dehaan, J. Louis, A. Wilson, A. Hall, and R. Rumbachs, "Discrimination of blackberry (*Rubus fruticosus* sp. agg.) using hyperspectral imagery in Kosciuszko National Park, NSW, Australia," *ISPRS J. Photogramm. Remote Sens.*, vol. 62, no. 1, pp. 13–24, 2007.
[47] J. M. Peña-Barragan, F. Lopez-Granados, M. Jurado-Exposito, and L. Garcia-Torres, "Mapping *Ridolfia segetum* patches in sunflower crop using remote sensing," *Weed Res.*, vol. 47, no. 2, pp. 164–172, Apr. 2007.
[48] J. Mielikainen and P. Toivanen, "Lossless compression of hyperspectral images using a quantized index to lookup tables," *IEEE Geosci. Remote Sens. Lett.*, vol. 5, no. 3, pp. 474–478, Jul. 2008.
[49] B. Somers, K. Cools, S. Delalieux, J. Stuckens, D. Van der Zande, W. W. Verstraeten, and P. Coppin, "Nonlinear hyperspectral mixture analysis for tree cover estimates in orchards," *Remote Sens. Environ.*, vol. 113, no. 6, pp. 1183–1193, Jun. 2009.

Ben Somers (S'09) received the M.Sc. degree in bioscience engineering (land and forest management) in 2005 from the Katholieke Universiteit Leuven (K.U. Leuven), Leuven, Belgium, where he is working toward the Ph.D. degree with the Geomatics Engineering Group, Department of Biosystems.

Since 2006, he has been a Research Associate with K.U. Leuven. His research interests include the design of processing tools for hyperspectral remote sensing with a specific focus on spectral mixture analysis.

Stephanie Delalieux received the Ph.D. degree in applied bioscience and engineering from the Katholieke Universiteit Leuven, Leuven, Belgium, in 2009.

She is currently a Postdoctoral Research Fellow with the Centre for Remote Sensing and Earth Observation processes (TAP), Flemish Institute for Technological Research (VITO), Mol, Belgium. Her research interests include the development of hyperspectral indices for presymptomatic detection of stress in fruit trees and the development of hyperspectral image analysis techniques for habitat classification.

Willem W. Verstraeten received the M.Sc. degree in agriculture engineering and the Ph.D. degree from the Katholieke Universiteit Leuven (K.U. Leuven), Leuven, Belgium, in 1999 and 2006, respectively, with emphasis on estimating evapotranspiration, soil moisture, and carbon sequestration using satellite remote sensing data.

He is currently the Research Team Leader of the Geomatics Engineering Group, Department of Biosystems, K.U. Leuven. He manages scientific research in the field of hyperspectral remote sensing to detect vegetation stress, BRDF modeling, spectral unmixing of vegetation and soil signals, plant production systems, spaceborne time-series analysis, and LiDAR data applications. He received a fellowship to carry out studies at the Flemish Institute for Technological Research (VITO).

Jan Verbesselt received the Ph.D. degree in applied bioscience and engineering from the Katholieke Universiteit Leuven, Leuven, Belgium, in 2006.

He is currently a Postdoctoral Research Fellow with the Commonwealth Scientific and Industrial Research Organisation Sustainable Ecosystems, Clayton South, Australia. He is the author or a coauthor of several published articles on spatio-temporal analysis of high temporal, spectral, and spatial remotely sensed data to derive biophysical variables, phenological metrics, trends, and seasonality. His main research interests include change detection and time-series analysis of high spatial and temporal satellite data.

Stefaan Lhermitte received the M.Sc. and Ph.D. degrees from the Katholieke Universiteit Leuven, Leuven, Belgium, in 2002 and 2008, respectively.

During his Ph.D. studies, he focused on spatio-temporal patterns of vegetation growth after wildfires. He is currently with the Centro de Estudios Avanzados en Zonas Aridas (CEAZA), La Serena, Chile, where his work focuses on the use of remote sensing for studying climate oscillations. His research interests include the use and development of time-series analysis and spatio-temporal classification techniques for remote sensing applications in climatological, cryospheric, and ecological studies.

Pol Coppin received the B.Sc. and M.Sc. degrees in forest engineering from Belgium and the Ph.D. degree in forest resources from the University of Minnesota, Minneapolis.

He is currently the Dean of the Faculty of Bioscience Engineering and the Chair Professor of geomatics engineering with the Katholieke Universiteit Leuven, Leuven, Belgium. He is the Project Leader on the Flemish side for the joint Flemish–South African IS-HS program and is responsible for the hyperspectral sensor, the electronic bundle-steered antenna, the transponder technology for on-board communication with ground sensor suites, and the integrated monitoring and modeling of plant systems. His career spans 12 years of professional experience (and many short-term missions afterward) in tropical and subtropical natural resources assessment and monitoring (1977–1988), followed by an academic career in the U.S. at the University of Minnesota, Minneapolis, and Purdue University, West Lafayette, IN (1988–1995), and in Belgium at K.U. Leuven (1995 up to present).

Authorized licensed use limited to: UNIVERSIDAD DE LA SERENA. Downloaded on October 26, 2009 at 07:46 from IEEE Xplore. Restrictions apply.